Microfluid Nanofluid (2014) 17:233–244
DOI 10.1007/s10404-013-1290-x

RESEARCH PAPER

Effect of solvent composition on the structural and magnetic properties of MnZn ferrite nanoparticles obtained by hydrothermal synthesis

R. M. Freire · P. G. C. Freitas · T. S. Ribeiro · I. F. Vasconcelos · J. C. Denardin · G. Mele · L. Carbone · S. E. Mazzetto · P. B. A. Fechine

Received: 13 July 2013 / Accepted: 11 November 2013 / Published online: 24 November 2013

Abstract Samples of manganese–zinc (MnZn) ferrites were successfully prepared by hydrothermal syntheses using different compositions of the reactive system $(H_2O)_{1-x}$:$(EG)_x$ ($x = 0$, 0.2, 0.4, 0.6, 0.8, and 1.0), where EG = ethylene glycol. The samples were fully investigated by powder X-ray diffraction, Fourier transform infrared spectroscopy for both liquid and solid specimens, Mössbauer spectroscopy, vibrating sample magnetometer, and transmission electron microscopy. All the MnZn ferrites presented spinel phase and average particle diameters between 3.1 and 12.1 nm. The increase in the x values results in a decrease in the particle sizes. The FTIR spectra performed in liquid phase showed significant interaction between EG and metallic precursors used in the synthesis. Magnetic features as for instance saturation magnetization (M_S) also decreases upon increasing the x values. In addition, all synthesized samples exhibited a superparamagnetic character at room temperature. The experimental methodology presented in this work is used to obtain superparamagnetic nanoparticles with controlled size (smaller than 13 nm) and morphology.

Keywords Magnetic nanoparticles · MnZn ferrite · Ethylene glycol · Hydrothermal synthesis

R. M. Freire · P. G. C. Freitas · S. E. Mazzetto · P. B. A. Fechine (✉)
Grupo de Química de Materiais Avançados (GQMAT), Departamento de Química Analítica e Físico-Química, Universidade Federal do Ceará (UFC), Campus do Pici, CP 12100, Fortaleza, CE CEP 60451-970, Brazil
e-mail: fechine@ufc.br

T. S. Ribeiro · I. F. Vasconcelos
Departamento de Engenharia Metalúrgica e de Materiais, Universidade Federal do Ceará, Fortaleza, CE, Brazil

J. C. Denardin
Departamento de Física, Universidad de Santiago de Chile, USACH, Av. Ecuador 3493, Santiago, Chile

G. Mele
Dipartimento di Ingegneria dell'Innovazione, Università del Salento, Via Arnesano, 73100 Lecce, Italy

L. Carbone
NNL, Istituto Nanoscienze UOS Lecce, Via Arnesano 16, 73100 Lecce, Italy

1 Introduction

In the last decades, magnetic materials have been the subject of intensive investigations due to their inherent magnetic properties and applications in electronic devices, such as inductors, AC/DC converters, transformers, noise filters, recording heads, and others (Zhang et al. 2009; Poddar et al. 2005). This kind of material also have generated a lot of interest in biomedical applications (Barreto et al. 2013; Boyer et al. 2010; Arruebo et al. 2007) for magnetic contrast resonance imaging (MRI), magnetic separation, targeted drug delivery, tissue engineering, cell tracking, bioseparation, and magnetic hyperthermia. Thus, the advancement of nanotechnology has brought new strategies and perspectives mainly for medicine (Botelho et al. 2009, 2010, 2013; Gonzaga et al. 2012). In this way, manganese–zinc ferrites (MnZn) assume special importance due to their chemical composition and crystal structure, with the metal ions distributed among eight tetrahedral (A) and 16 octahedral (B) coordinated sites per unit cell, in which oxygen atoms form a face-centered cubic (FCC) lattice. These characteristics lead to a material with high initial permeability and saturation magnetization, as well as lower eddy current loss compared with alloy

cores (Sharifi et al. 2012). Apart from being interesting for electronic devices, MnZn ferrites have been also used for biomedical applications and furthermore demonstrating to be potentially promising for MRI, drug delivery, and magnetic fluid hyperthermia (Latorre-Esteves et al. 2009).

In order to obtain good magnetic and structural properties, several methodologies were developed to synthesize magnetic nanoparticles (MNP): as for instance microemulsion-based methods (Pérez et al. 1997), sol–gel syntheses (Dai et al. 2005), co-precipitation (Barreto et al. 2013; Velmurugan et al. 2010), and hydrothermal reactions (Srivastava et al. 2009; Freire et al. 2013). These methods provide MNP with different and tunable shapes (nanospheres, nanorods, etc.), size, structural, and magnetic properties. Among these methodologies, the hydrothermal approach has been commonly used as a favorable route to synthesize spinel ferrites. This technique allows obtaining a variety of ceramics and offers many advantages over other conventional and non-conventional procedures. The nanoparticles (NP) nucleate directly in the solution leading to the materials of high purity and crystallinity (Suchanek and Riman 2006). Moreover, the rate and uniformity of nucleation and growth can be modeled by thermodynamic variables (temperature, reactant concentrations, various additives, and/or solvents). The liquid phase allows for parameter changes as diffusion, adsorption, reaction rate, and others (Riman et al. 2002). This improves the size and morphology control of crystallites and significantly reduces the extent of NP aggregation. Then, the choice of the reaction environment (solvent or mixtures) in which the NP will be produced is extremely important. Nevertheless, the literature (Yáñez-Vilar et al. 2009; Pérez-Mirabet et al. 2013) reports few studies evaluating the role of different solvents in the synthesis of MNP under solvo/hydrothermal conditions. The majority of papers evaluate how the experimental conditions as temperature (Mozaffari et al. 2010), stirring velocity (Valenzuela et al. 2009), and precipitating agent (Aquino et al. 2002) may affect the particle size and morphology. However, another strategy largely employed by the researchers is the use of stabilizing agents such as oleic acid (Zhang et al. 2006) and sodium acetate (Wang et al. 2009), oleylamine (Pérez-Mirabet et al. 2013), and polysaccharides (carboxymethyl cellulose sodium) (Chang et al. 2011).

In the present work, $MnZnFe_2O_4$ nanoparticles were prepared under hydro/solvothermal conditions in different solvent compositions of water and/or EG. We show a dependency of the magnetic and structural properties on the changes of solvent compositions. Structural, optical, and magnetic features of the produced nanoparticles were studied by XRD, TEM, FTIR, Raman and Mössbauer spectroscopies, and vibrating sample magnetometry.

Table 1 x Values and label of the samples obtained in this work

x	Label
0.0	EG0
0.2	$(H_2O)_{0.8}$:$(EG)_{0.2}$
0.4	$(H_2O)_{0.6}$:$(EG)_{0.4}$
0.6	$(H_2O)_{0.4}$:$(EG)_{0.6}$
0.8	$(H_2O)_{0.2}$:$(EG)_{0.8}$
1.0	EG1

2 Experimental

2.1 Materials and methods

All reagents were commercial products with analytical grade and employed without further purification. The chemical reagents for this work are ferric chloride hexahydrate ($FeCl_3{\cdot}6H_2O$, Dinâmica, 97 %) manganese chloride tetrahydrate ($MnCl_2{\cdot}4H_2O$, Vetec, 99 %), zinc chloride ($ZnCl_2$, Dinâmica, 97 %), sodium hydroxide (NaOH, Cinética Química, 97 %), and EG ($C_2H_6O_2$, Reagen, P.A.).

2.2 Synthesis of $MnZnFe_2O_4$ nanoparticles

$MnZnFe_2O_4$ nanoparticles were synthesized according to Lee et al. (1999). However, some modifications were performed, as follows. Stoichiometrically required amounts of metallic reagents were dissolved in a beaker under different proportions of $(H_2O)_{1-x}$:$(EG)_x$ $(0 \leq x \leq 1)$. All of the x values used for the samples' preparation are summarized in Table 1. Under vigorous mechanical stirring, it was prepared a mixture of 1.85 mmol of $MnCl_2{\cdot}4H_2O$, 1.85 mmol of $ZnCl_2$, and 7.4 mmol of $FeCl_3{\cdot}6H_2O$. NaOH ($\sim$37.5 mmol) was added into the mixture in order to precipitate the desired hydroxides. The as-obtained slurry was sealed in a Teflon-lined stainless steel autoclave, and the crystallization was carried out under autogenously pressure at temperature of 250 °C for 0.5 h. The reaction occurring during this process can be summarized as follows:

$$0.5Mn^{2+} + 0.5Zn^{2+} + 2Fe^{3+} + 8OH^- \rightarrow Zn_{0.5}M_{0.5}Fe_2O_4 + 4H_2O \quad (1)$$

After this procedure, the autoclave was cooled down to room temperature and the precipitate washed several times with water and methanol. The materials were then dried in air at 100 °C for 3 h. The MNP resultant was labeled according to the x values, which indicate the amount of EG contained in the solvent.

2.3 Stabilization of the metallic precursors from EG

The stabilizing role of EG relatively to the metal chlorides employed in the MnZn ferrite synthesis was tested separately at the same conditions of reagent's concentration and

temperature. Each metallic salt was loaded into a 10-mL glass flask containing the system $(H_2O)_{1-x}$:$(EG)_x$ in different proportions ($x = 0$, 0.2, 0.4, 0.6, 0.8, and 1.0). After this step, NaOH was added dropwise under continuous magnetic stirring. The products obtained were investigated by Infrared—FT Raman Vertex 70 Bruker equipped with a PIKE MIRacle^{TM} ATR accessory.

2.4 Characterization of the MNP

The structural analysis was made by X-ray powder diffraction (XRD) patterns of the obtained samples using CuKα (1.54056 Å) from a Rigaku diffractometer with a Bragg–Brentano geometry in the range of 20°–70° angle degrees. The phase identification was made by comparing powder diffractograms with standard patterns from International Centre for Diffraction Data (ICDD). Rietveld refinement procedures (Maia et al. 2008; Rietveld 1967) were applied to all diffraction patterns using the DBWS 2.25 (Bleicher et al. 2000). The infrared spectra (FTIR) of the samples were carried out on a PerkinElmer Fourier transform infrared spectrometer in the range 4,000–400 cm^{-1}. In recording FTIR spectra, each sample was mixed with potassium bromide (KBr) powder and pressed into pellets. The Mössbauer spectrum was recorded at room temperature (300 K) from *FAST* (*ConTec*) *Mössbauer System* spectrometer using transmission geometry. A ^{57}Co radioactive source was used. The data analysis was performed using NORMOS program written by R.A. Brand (distributed by Wissenschaftliche Elektronik GmbH, Germany). Isomer shifts (δ) are referred to α-Fe at room temperature. Magnetic properties were investigated by a vibrating sample magnetometer (VSM) Mini 5 Tesla from Cryogenic Ltd. The VSM has been previously calibrated using a YIG sphere, and after measuring the mass of each sample, the magnetization was given in emu/g. Microstructural studies including the evaluation of particle size and morphology were performed on a Jeol JEM-1011 electron microscope operating at 100 kV, equipped with a CCD camera ORIUS 831 from Gatan. Transmission electron microscope (TEM) images of the samples were prepared by drop-casting dilute nanocrystal solutions onto carbon-coated copper grids. Afterward, the deposited samples were allowed to complete dry at 60 °C for one night before examination.

3 Results and discussion

3.1 X-ray diffraction (XRD)

Figure 1 shows the XRD patterns for all samples synthesized under different conditions of composition of water and ethylene glycol. Black dots in the figure represent the observed (Obs) data collected from experimental measurements. On the other hand, red lines correspond to the calculated (Calc) data obtained from the computational processing performed by the Rietveld method, while the green lines represent the relative difference (Dif) between them. The diffraction peaks assigned to (220), (311), (400), (422), (511), and (440) planes can be attributed to cubic phase (ICDS, file no. 017-0912) with spatial group O_h^7. However, the sample with $x = 0.8$ ($(H_2O)_{0.2}$:$(EG)_{0.8}$) exhibits a peak at 33.2°, which indicates the presence of the hematite phase (α-Fe_2O_3) (ICSD, file no. 071-0469). This phase may be explained by Fe^{3+} migration out of the spinel structure (Paiva et al. 2008). Generally, calcination is a necessary step in the preparation of ferrites by chemical methods (Zhang et al. 2009). Moreover, the calcination temperature plays a key role in the determination of final crystal structure and particle size (Lv et al. 2008). The XRD results showed that only samples subjected to hydrothermal treatment performed during synthesis exhibit diffraction peaks characteristics of the spinel phase.

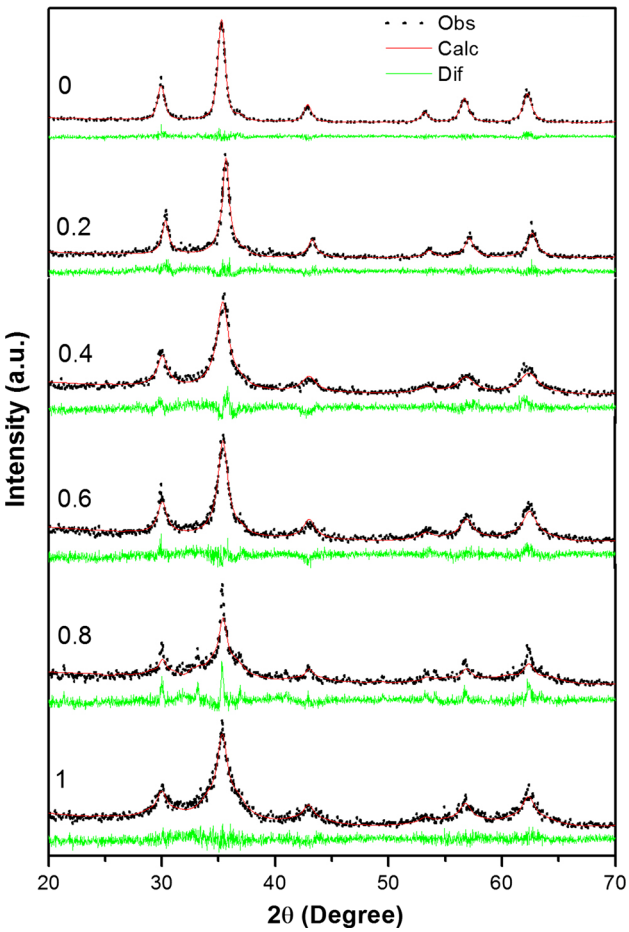

Fig. 1 XRD for samples of the system $(H_2O)_{1-x}$:$(EG)_x$. The corresponding x values are reported in each diffractogram

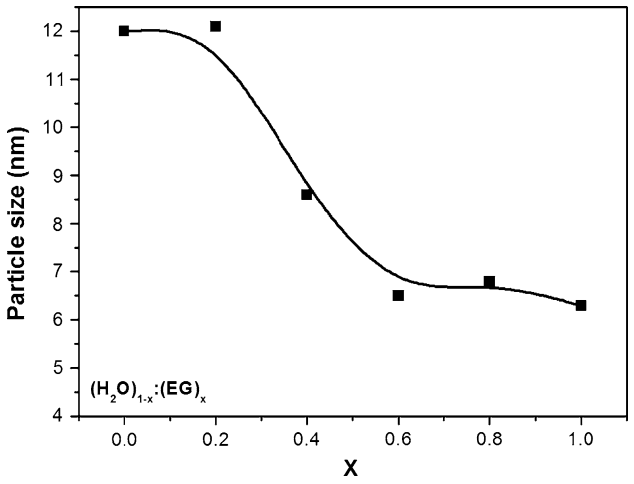

Fig. 2 Particle size describes in function of the x values

Thereby, a calcination step was not necessary for all samples synthesized in this work. This highlights the efficiency of the synthesis process furthermore providing particles of small size, since for MnZn ferrites the average crystalline size generally increases by increasing the calcination temperature due to crystallites coalescence at high temperatures (Raming et al. 2002; Maaz et al. 2007). In addition, the presence of EG may play the role of a complexing agent stabilizing particle's dispersibility in solution their small dimensions. Similar studies in the literature corroborate this effect played by polyols (Caruntu et al. 2002; Poul et al. 2003; Chkoundali et al. 2004; Knetsch and Groeneveld 1973).

The average crystallite size was calculated using the Debye–Scherrer equation after accounting for instrumental broadening (Rietveld method) (Velmurugan et al. 2010). These values are plotted as a function of EG fraction (Fig. 2). It was possible to observe a decrease in average crystallite sizes when the EG fraction in the reactive domain raises. Interestingly, the size reduction sharply climbs ($\sim$30 %) as the EG fraction exceeds 0.2. Then, after a x value of 0.5, it levels out again due to a less pronounced crystallite size reduction. This trend suggests the existence of a minimum threshold concentration in which EG can stabilize a maximum number of nanoparticles in solution, thus contributing to decrease the average sizes of the samples.

3.2 Stability of metallic chlorides with EG

Tests of solubility of the diverse metallic precursors individually dispersed in solutions exhibiting different compositions of water-to-ethylene glycol ($(H_2O)_{1-x}$:$(EG)_x$) have been performed. These experiments were carried out in order to investigate the influence of EG on the stability of Mn^{2+}, Zn^{2+}, and Fe^{3+} chlorides in phase solution. Each metallic chloride was solubilized in 5 mL of solvent with different amounts of EG ($x = 0$, 0.2, 0.4, 0.6, 0.8, and 1.0). The same solubilizing procedure was applied to anhydrous NaOH that works as a precipitating agent of formed nanoparticles in the synthesis. Upon mixing both solutions, possible precipitation can be observed depending on the x values. Figure 3 summarizes the final outcomes. Relatively to Mn and Fe, a solid precipitate was noted in the case of solutions containing 0 or 0.2 of EG fraction. When this concentration was exceeding, it was observed only color changes without any solid precipitation. Differently, Zn-based salt did not show any changes of color or precipitate formation as a function of EG fraction. This result confirmed the improved dispersibility of particles in solution due to the increase in EG fraction. Literature reports that EG can behave as a mono or bidentate ligand (Knetsch and Groeneveld 1973). Therefore, to evaluate the interaction of metallic precursors with EG, it was performed FTIR spectra of solutions resultant after adding of the NaOH. Figure 4 shows the spectrum for each test realized with different x values and metallic precursors. It is possible to observe a similarity for all spectra with bands around 3,350 and 1,640 cm^{-1} for sample with $x = 0$, characteristic of the stretch and bending O–H of water molecules, respectively. However, for the tests performed with $x \neq 0$, the same band clearly shows shift to lower frequencies ($\sim$3,300 cm^{-1}). This indicates the coordination of EG with metallic precursors by oxygen atoms. The bands referring to the stretch of CH_2 near 3,000 cm^{-1} showed no displacement. The bands were observed at 1,082 and 1,036 cm^{-1}, which can be attributed to CH_2 rocking vibrations. No splittings were observed, and both bands show shift of $\sim$10 cm^{-1} to lower frequencies (Miyake 1959). This evidences the bidentate coordination, but the shape of the spectra in the ranges 1,700–1,200 cm^{-1} with a series of bands contradicts such a claim (Knetsch and Groeneveld 1973). A bending COH was also observed indicating monodentate coordination. Therefore, the results showed in this section indicated a strong interaction of EG with metal chlorides and minimal concentration close to 0.4 for the stabilization of the precursors in solution. This may explain the decrease in average crystallite size from that concentration observed in the results of XRD.

3.3 Infrared spectroscopy

As reported before, it was possible to confirm the presence of spinel phase in all samples from the results of XRD. According to the literature (Shebanova and Lazor 2003), this phase contains two distinct cationic lattice positions namely tetrahedral and octahedral sites coordinated by oxygen anions. Both sites contributes to the active modes in IR, and a theoretical analysis based on the nuclear site

Fig. 3 Results of the stabilization test for different precursors metallic used in the synthesis. On the *left side* of each series of tests, the relative metal is reported. The x values for the system $(H_2O)_{1-x}$:$(EG)_x$ are presented only in the case of Zn series, but can be straightforwardly expanded for Mn and Fe

group approach (Porto 1981) predicts four IR-active bands T_{1u} (Gupta et al. 2002). Figure 5 shows the FTIR spectra in the range 4,000–400 cm^{-1} for all samples. It can be observed two bands in the range 650–400 cm^{-1} widely observed for ordered spinel ferrites (Bezerra 2007; Ravinder 1999). The absorption bands observed in the range 600–550 and 450–385 cm^{-1} can be attributed to the tetrahedral and octahedral sites, respectively (Barreto et al. 2011; Freire et al. 2013). It is important to note that in the working range it is possible to observe only two modes. These results are in agreement with the literature (Freire et al. 2012, 2013; Thomas and George 2009).

The different position of the absorption bands attributed to octahedral and tetrahedral sites gives key indications relatively to the insertion or mobility of cations into network spinel (Dawoud 2006). The interaction between oxygen and cations strongly affects the wavelength values observed in Fig. 5. According to the literature (Amer et al. 2011), bands frequency are proportional to the force constant (K), which can be calculated using the relation:

$$v = \frac{1}{2\pi}\sqrt{\frac{K}{\mu}} \tag{2}$$

where μ is the reduced mass and v the frequency. The values of v_O, v_T, K_o, and K_T for all samples are listed in the Table 2, where subscripts O and T means octahedral and tetrahedral, respectively. Figure 6 shows the K values plotted as a function of EG fraction. As a general trend, it was clear that the force constants' values increase with EG fraction in the system, which was accompanied by the decrease in the particle size. The literature (Choi et al. 2005) reports that a volume contraction occurs within the nanoparticles due to the decrease in particle size. This leads to increase in the force constants as a result of the decreases in the interatomic distances. Then, the behavior observed can be assigned to the decrease in metal–oxygen bond lengths at the octahedral and tetrahedral sites. Moreover, K values can be too influenced by the method of preparation and porosity (Reddy and Salagram 1987; Waldron 1955; Josyulu and Sobhanadri 1981). The same relationship

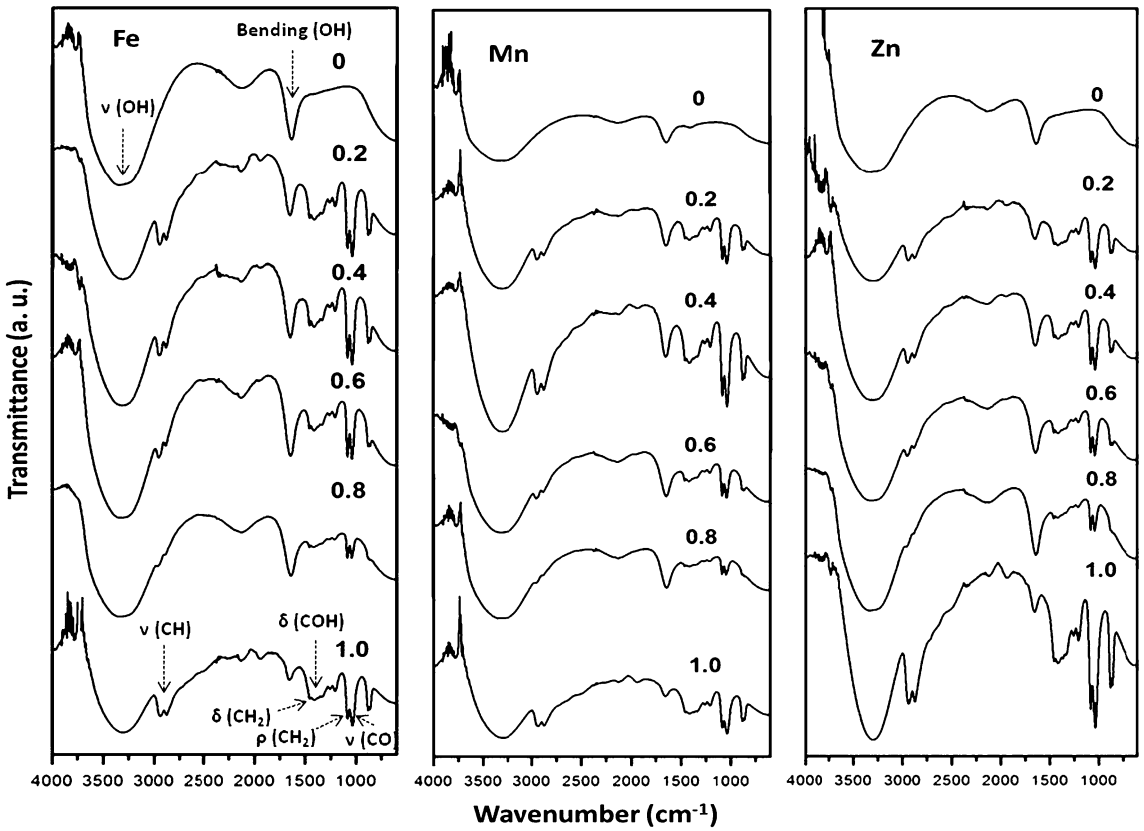

Fig. 4 IR spectra of the tests realized with different x in the system $((H_2O)_{1-x}:(EG)_x)$ for metallic precursors

between K values and EG fraction was observed for both sites. This indicates that increase in the EG fraction did not cause the mobility of cations into spinel network. However, the same conclusion cannot be inferred for sample synthesized with $(H_2O)_{0.2}:(EG)_{0.8}$. It was seen a decrease in K_T values and increase for K_o. These changes can be attributed to the weakening in metal–oxygen bond at the tetrahedral site due to the mobility of cations into network spinel. Migrations of cations with small ionic radius from tetrahedral to octahedral sites lead the shifts of K_o toward high values due to increase in the metal–oxygen interaction. This may be related to the Fe^{3+} displacement from tetrahedral to octahedral sites. Similar effect was observed for MgZn ferrite (Mohammed et al. 2012). Furthermore, the XRD results for $(H_2O)_{0.2}:(EG)_{0.8}$ have shown α-Fe_2O_3. As previously reported, the presence of this phase can be attributed to the migration of Fe^{3+} out of the spinel structure (Paiva et al. 2008). This may have generated an energetic imbalance into network spinel contributing to the mobility of Fe^{3+} for octahedral sites.

3.4 Mössbauer spectroscopy

Figure 7 shows Mössbauer spectrum at room temperature of the samples of the $(H_2O)_{1-x}:(EG)_x$ system. The dots represent the experimental data, while solids lines illustrate least-squares fitting. All synthesized samples presented strong superparamagnetic characteristics due to their particle size (Knobel et al. 2008), which was evidenced by a doublet at the center of the spectra (Wang and Li 2001; Siddique and Butt 2010). When the sizes decrease, the thermal energy strongly contributes to the collapse of the magnetic ordering and the superparamagnetic relaxation phenomenon is observed. Furthermore, it is interesting to note that for samples with fraction (x) between 0 and 0.6, it was needed to add sub-spectrum (continuous lines in different colors inside each spectrum) for a better fit to the baseline. This corresponds to different environments at the iron nucleus. As reported above, the doublet (orange line) corresponds to Fe atoms into small particles with superparamagnetic character. It was also found a V-shaped subspectrum (blue line). This can be explained by the substitution of manganese ions with those of zinc, weakening the magnetic interactions, thus reducing A–B sites coupling pairs (Upadhyay et al. 2003). The said sub-spectrum V-shaped was gradually disappearing with increase in EG fraction.

Hyperfine parameters are presented at Table 3. The isomer shifts (δ) remained between 0.31 and 0.34 mm/s. These values can be attributed at high-spin Fe^{3+} state

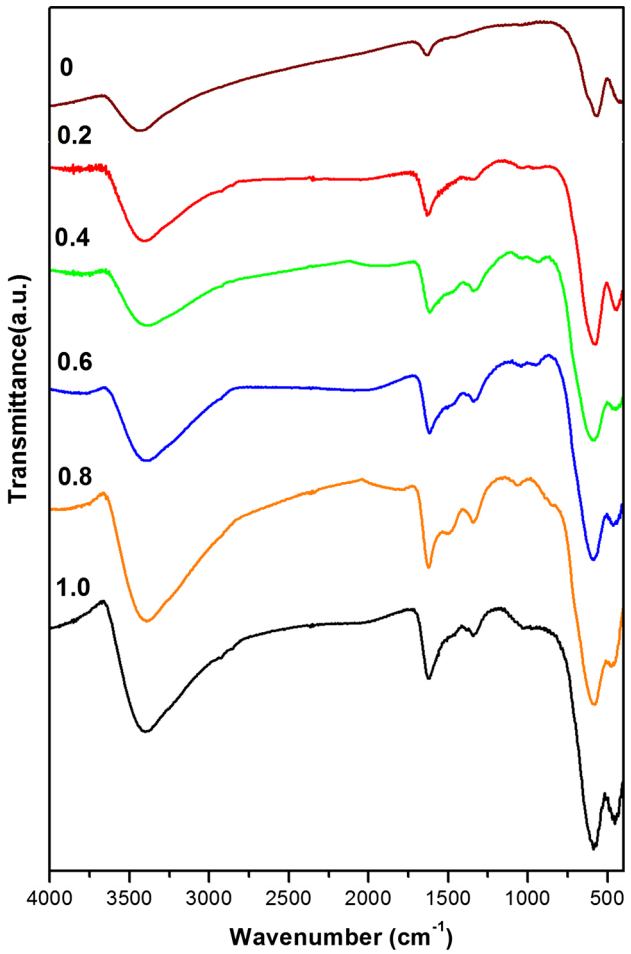

Fig. 5 FTIR for samples of the system $(H_2O)_{1-x}$:$(EG)_x$

Table 2 Values of x, v_T, v_O, K_o, and K_T for all samples synthesized

Samples	x	v (cm^{-1})		$K \times 10^3$ (dyne cm^{-1})	
		v_T	v_O	K_T	K_O
EG0	0.0	566.9	419.3	239.2	135.1
$(H_2O)_{0.8}$:$(EG)_{0.2}$	0.2	580.3	446.1	250.7	143.2
$(H_2O)_{0.6}$:$(EG)_{0.4}$	0.4	591.0	451.4	258.1	148.9
$(H_2O)_{0.4}$:$(EG)_{0.6}$	0.6	592.3	450.9	258.1	148.9
$(H_2O)_{0.2}$:$(EG)_{0.8}$	0.8	588.4	459.5	251.8	160.5
EG1	1.0	585.6	454.8	258.8	152.0

(Dickson and Berry 1986). The average δ for all samples appears to show no significant variation with EG fraction, since this parameter is inherent to the oxidation state of the Fe atom. In order to obtain the best fit of the experimental data for quadrupole interaction (Δ), it was performed using a distribution of probable values for this parameter. The resulting distribution graphs are shown beside each sample, and the peak of greatest intensity shows the most likely value. Thus, it can be seen that for all samples, the Δ has

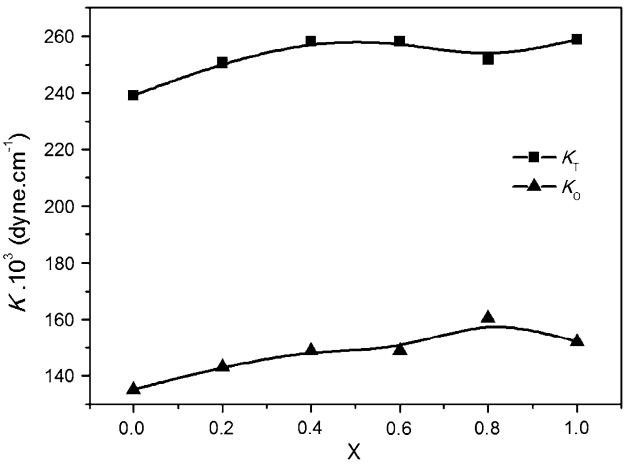

Fig. 6 K values for tetrahedral (K_T) and octahedral (K_O) site plotted as a function of x

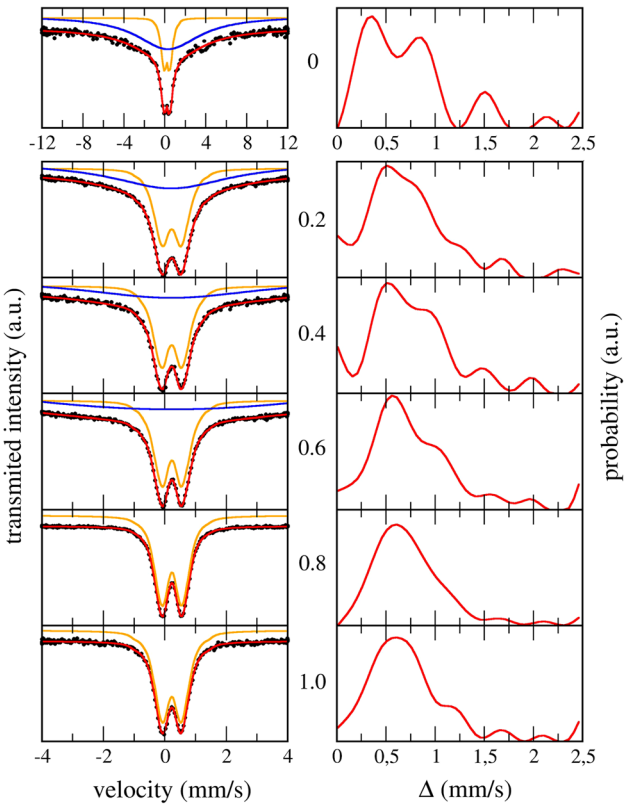

Fig. 7 Mössbauer spectra (*left*) and quadrupole (Δ) distribution (*right*) for samples of the system $(H_2O)_{1-x}$:$(EG)_x$ (color figure online)

values in the range 0.3–0.6 mm/s. The relatively high values of Δ can be assigned to the chemical disorder and the local symmetry reduction in site (Singhal et al. 2006; Ying et al. 1992). Moreover, the broad distribution and the presence of peaks at lower intensities also reflect the high degree of disorder of the structures (Sorescu et al. 2004). Interestingly, these peaks appear to be attenuated with

Table 3 Hyperfine parameter for samples synthesized in this work

Samples	Hyperfine parameters δ (mm/s)[a]
EG0	0.31
$(H_2O)_{0.8}$:$(EG)_{0.2}$	0.33
$(H_2O)_{0.6}$:$(EG)_{0.4}$	0.33
$(H_2O)_{0.4}$:$(EG)_{0.6}$	0.34
$(H_2O)_{0.2}$:$(EG)_{0.8}$	0.34
EG1	0.34

[a] For all the samples, δ measured relative to α-Fe

increasing x values. Therefore, a decrease in the degree of disorder of the structure can be observed. However, this effect was better viewed for $x \geq 0.4$ due to the stabilization of metallic precursors founded for theses values. Thus, clearly the increase in the EG fraction contributes to a structural homogeneity site Fe.

3.5 Magnetic measurements

The magnetic properties of the nanoparticles synthesized in this work were measured as a function of the field and temperature. The results of magnetization curves measured at 300 K are presented in Fig. 8. The magnetization curves almost did not present coercivity and remanence at room temperature. This fact points for relaxation superparamagnetic phenomenon (Knobel et al. 2008) in agreement with the results of Mössbauer spectroscopy. It is also noted a decrease in saturation magnetization (M_S) for increasing values of x. According to the literature (Sato et al. 1987), the decrease to the M_S occurs due to the presence of a magnetically inactive layer or non-collinear spin arrangement on surface of the particles (Leung et al. 1973). Furthermore, this reduction can be attributed to the higher surface-to-volume ratio arising from small particles being

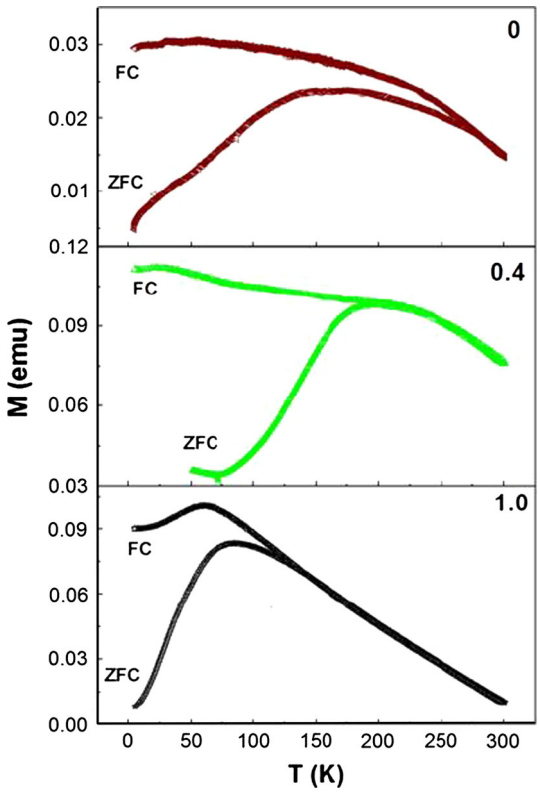

Fig. 9 Zero field-cooled/field-cooled curves of samples with $x = 0$, 0.4, and 1.0

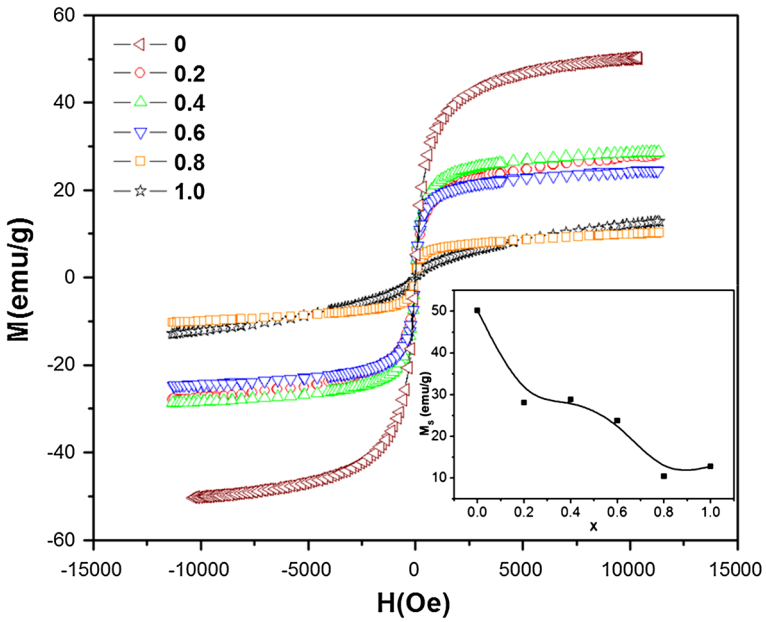

Fig. 8 Magnetic measurements for samples of the system $(H_2O)_{1-x}$:$(EG)_x$. *Inset* reports plotted as a function of the

present in these samples. Since the contribution of the non-magnetic layer located at the surface is greater as the particle size decreases (Sánchez et al. 2002). The inset of Fig. 8 shows the isothermal behavior of M_S as a function of the EG fraction (x). It is possible to observe that M_S decreases almost linearly with increasing of the x values. In general, XRD data show that the particle size follows an inversely proportional relationship with x values. Therefore, the result observed here was expected due to greater contribution of the non-magnetic layer. However, the sample $(H_2O)_{0.2}$:$(EG)_{0.8}$ presents abnormality with low M_S value compared with EG1. This can be explained by the presence of the α-Fe_2O_3 (non-magnetic phase) in the sample $(H_2O)_{0.2}$:$(EG)_{0.8}$, as detected by XRD (Fig. 1). Similar results can be found in the literature (Freire et al. 2012; Laokul et al. 2011; Sugimoto 1999). Figure 9 shows the zero field-cooled (ZFC)/field-cooled (FC) curves measured at a field of 50 Oe for three representative samples, with $x = 0$, 0.4, and 1.0 (selected samples). From these curves, it is shown that sample EG1 has a blocking temperature close to 75 K, where there is a maximum in the ZFC curve, and this temperature is where the nanoparticles

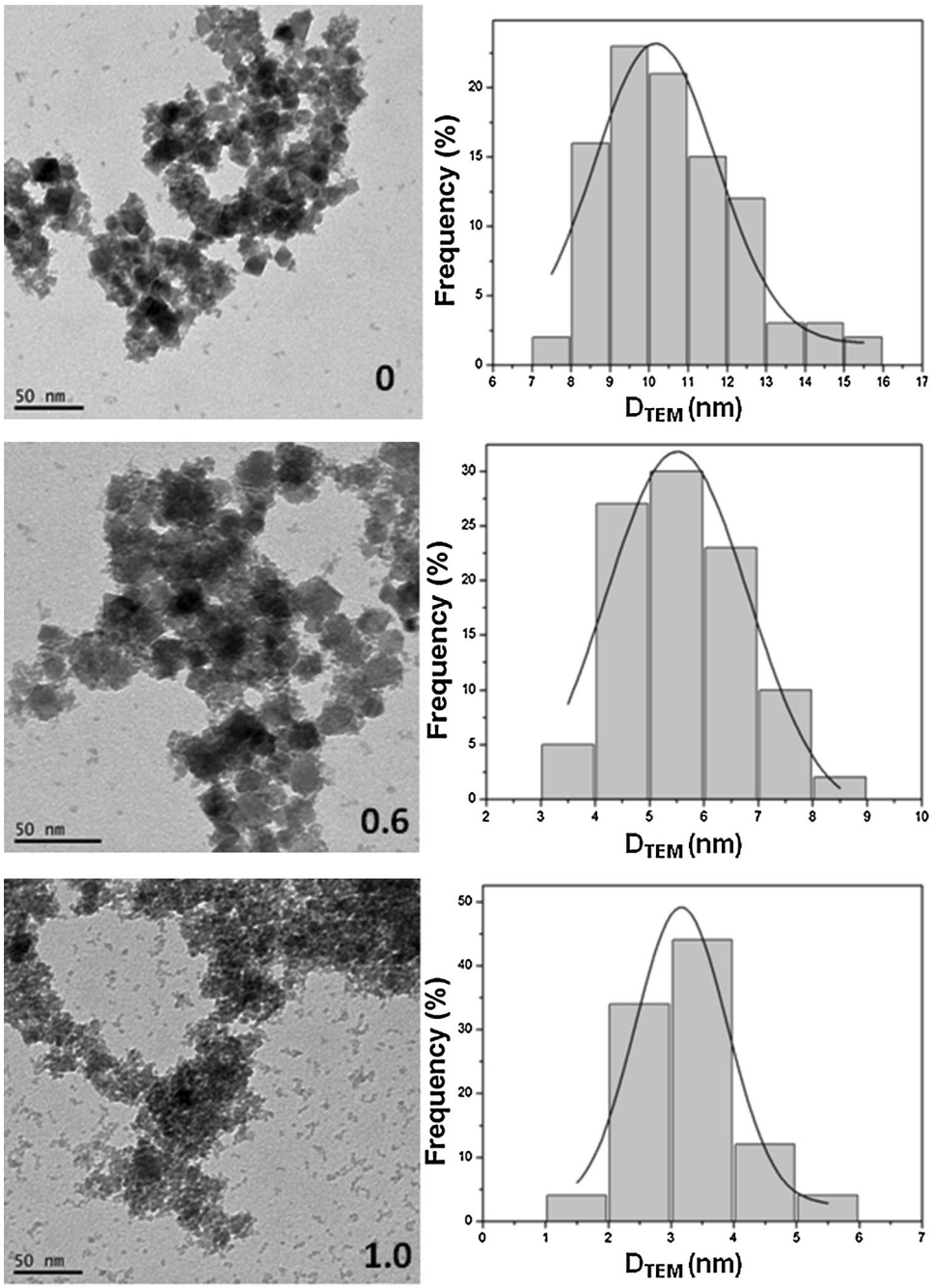

Fig. 10 TEM micrographs for samples of the system $(H_2O)_{1-x}$:$(EG)_x$

have a transition from the blocked state to a superparamagnetic state. The blocking temperature is observed to increase for larger nanoparticles (Hassnain Jaffari 2012). The samples with lower EG concentrations have larger values of blocking temperature, as shown in the ZFC–FC curves, in agreement with the results of particle sizes obtained by XRD and TEM images (next section).

3.6 Transmission electron microscopy (TEM)

The morphology and particle size of the samples were studied in more detail by TEM analysis, as shown in Fig. 10 for the samples EG0, $(H_2O)_{0.4}$:$(EG)_{0.6}$ and EG1, respectively. Each TEM picture displays also sample size distribution as determined by analyzing 100 particles randomly selected in different regions of the TEM grid. Specifically, particles with an approximate cubic shape and an average edge length of 12 ± 3 nm were founded for the sample EG0. On the other hand, it is strongly evident from TEM micrographs of the samples $(H_2O)_{0.4}$:$(EG)_{0.6}$ and EG1 that the cubic form is not maintained in these cases and the average particle diameter dropped to 5.5 ± 2 and 3.1 ± 2, respectively. This result was in accordance with XRD data, which showed a decrease in the particle size upon increasing the x values, namely an increment in the content of EG in the reactive environment. Another interesting aspect which draws the attention is represented by the degree of particles aggregation perceptible from TEM investigation. Clearly, the samples $(H_2O)_{0.4}$:$(EG)_{0.6}$ and EG1 have a higher degree of particles aggregation than EG0. This can be explained by the fact that a decrease in the particle size entails a larger specific surface area and consequently higher surface energy (Feng et al. 2008). Hence, the samples $(H_2O)_{0.4}$:$(EG)_{0.6}$ and EG1 presented a higher number of aggregated particles in the TEM images.

4 Conclusion

Superparamagnetic MnZn ferrites with high crystallinity and average particle diameter within the range 3.1–12.1 nm were synthesized by hydrothermal conditions under different compositions of the system $(H_2O)_{1-x}$:$(EG)_x$ ($x = 0$, 0.2, 0.4, 0.6, 0.8, and 1.0). XRD and TEM results showed a decrease in average particle size as a function of the increase in x values. However, this effect becomes more effective for $x \geq 0.4$. In order to explain this, FTIR analysis suggested that EG molecules interact strongly with the original metal precursors ($FeCl_3 \cdot 6H_2O$, $MnCl_2 \cdot 4H_2O$, and $ZnCl_2$), and images showed in the Fig. 3 presented strong stabilization for $x \geq 0.4$. Thus, the solubilization and stabilization of metallic precursors in solution proved to be a factor of great influence on the control of the average particle diameter. Moreover, magnetic properties such as M_S demonstrated to be strongly dependent on the composition of the reaction environment in the extent that an increase in x values produces a decrease in saturation magnetization. This can be reasonably attributed to a decrease in the particle size. Additionally, the Mössbauer spectroscopy and magnetization measurements showed that all synthesized nanoparticles presented a superparamagnetic behavior at room temperature. Thus, the methodology herein presented has been proved being effective to obtain superparamagnetic nanoparticles with controlled size (smaller than 13 nm).

Acknowledgments This work was supported by CAPES, Funcap and CNPq (Brazilian agencies), and by Fondecyt 1110252; Millennium Science Nucleus, Basic and Applied Magnetism Grant No. P10-061-F, AFOSR FA9550-11-1-0347 and CONICYT BASAL CEDENNA FB0807 (Chilean agencies). L. Carbone acknowledges financial support by the Italian Ministry of Education, University and Research through the Project AEROCOMP (contract MIUR No. DM48391).

References

Amer MA et al (2011) Spectral studies of Co substituted Ni–Zn ferrites. J Magn Magn Mater 323(11):1445–1452

Aquino R et al (2002) Size control of MnFe2O4 nanoparticles in electric double layered magnetic fluid synthesis. J Magn Magn Mater 252:23–25

Arruebo M et al (2007) Magnetic nanoparticles for drug delivery. Nano Today 2(3):22–32

Barreto A et al (2011) Magnetic nanoparticles for a new drug delivery system to control quercetin releasing for cancer chemotherapy. J Nanopart Res 13(12):6545–6553

Barreto ACH et al (2013) Magnetic nanosystem for cancer therapy using oncocalyxone A, an antitomour secondary metabolite isolated from a Brazilian plant. Int J Mol Sci 14(9):18269–18283

Bezerra MJOS (2007) Síntese e Caracterização da ferrita de MnZn obtida pelo método dos citratos precursores in Química. Universidade Federal do Rio Grande do Norte, Natal

Bleicher L, Sasaki JM, Paiva CO (2000) Santos, development of a graphical interface for the Rietveld refinement program DBWS. J Appl Crystallogr 33(4):1189

Botelho MA et al (2009) Protective effect of locally applied carvacrol gel on ligature-induced periodontitis in rats: a tapping mode AFM study. Phytother Res 23(10):1439–1448

Botelho MA et al (2010) Nanotechnology in ligature-induced periodontitis: protective effect of a doxycycline gel with nanoparticules. J Appl Oral Sci 18:335–342

Botelho MA et al (2013) Effects of a new testosterone transdermal delivery system, biolipidb2®-testosterone in healthy middle aged men: a confocal Raman spectroscopy study. J Pharm Sci Innov 2(2):1–7

Boyer C et al (2010) The design and utility of polymer-stabilized iron–oxide nanoparticles for nanomedicine applications. NPG Asia Mater 2:23–30

Caruntu D et al (2002) Reactivity of 3d transition metal cations in diethylene glycol solutions. Synthesis of transition metal ferrites with the structure of discrete nanoparticles complexed with long-chain carboxylate anions. Inorg Chem 41(23):6137–6146

Chang PR et al (2011) Polysaccharides as stabilizers for the synthesis of magnetic nanoparticles. Carbohydr Polym 83(2):640–644
Chkoundali S et al (2004) Nickel ferrite nanoparticles: elaboration in polyol medium via hydrolysis, and magnetic properties. J Phys: Condens Matter 16(24):4357
Choi HC, Jung YM, Kim SB (2005) Size effects in the Raman spectra of TiO_2 nanoparticles. Vib Spectrosc 37(1):33–38
Clemente CS et al (2013) Porphyrin synthesized from cashew nut shell liquid as part of a novel superparamagnetic fluorescence nanosystem. J Nanopart Res 15(6):1–10
Dai Z, Meiser F, Mohwald H (2005) Nanoengineering of iron oxide and iron oxide/silica hollow spheres by sequential layering combined with a sol–gel process. J Colloid Interface Sci 288: 298–300
Dawoud H (2006) A structural study of Cu–Zn ferrites by infrared spectra. Al-aqsa J 10:247–262
Dickson DPE, Berry FJ (1986) Mössbauer spectroscopy. Cambridge University Press, United States of America
Feng B et al (2008) Synthesis of Fe3O4/APTES/PEG diacid functionalized magnetic nanoparticles for MR imaging. Colloids Surf A 328(1–3):52–59
Freire RM, Barreto ACH, Fechine PBA (2012) Nanopartículas Magnéticas: aplicações terapêuticas no combate ao cancêr. Revista ABM—Metalurgia, Materiais e Mineração 68:54–56
Freire RM et al (2013) $MZnFe_2O_4$ (M = Ni, Mn) cubic superparamagnetic nanoparticles obtained by hydrothermal synthesis. J Nanopart Res 15(5):1–12
Gonzaga LW et al (2012) Nanotechnology in hormone replacement therapy: safe and efficacy of transdermal estriol and estradiol nanoparticles after 5 years follow-up study. Lat Am J Pharm 31(03):442–450
Gupta R et al (2002) Raman study of stoichiometric and Zn-doped Fe_3O_4. Phys Rev B 65(10):104430
Hassnain Jaffari G (2012) Effect of particle size distribution on the magnetic properties γ-Fe2O3 nanoparticles. Mater Sci Eng, B 177(12):935–941
Josyulu OS, Sobhanadri J (1981) The far–infrared spectra of some mixed cobalt zinc and magnesium zinc ferrites. Phys Status Solidi (a) 65(2):479–483
Knetsch D, Groeneveld WL (1973) Alcohol as ligands. III. Complexes of ethylene glycol with some divalent metal halides. Inorg Chim Acta 7:81–87
Knobel M et al (2008) Superparamagnetism and other magnetic features in granular materials: a review on ideal and real systems. J Nanosci Nanotechnol 8:2836–2857
Laokul P et al (2011) Characterization and magnetic properties of nanocrystalline CuFe2O4, NiFe2O4, ZnFe2O4 powders prepared by the *Aloe vera* extract solution. Curr Appl Phys 11(1):101–108
Latorre-Esteves M et al (2009) Synthesis and characterization of carboxymethyl dextran-coated Mn/Zn ferrite for biomedical applications. J Magn Magn Mater 321(19):3061–3066
Lee JH et al (1999) The characteristics of Ni–Zn ferrite powder prepared by the hydrothermal process. J Mater Sci Lett 18(13):1029–1031
Leung LK, Evans BJ, Morrish AH (1973) Low-temperature Mossbauer study of a nickel–zinc ferrite: $Zn_xNi_{1-x}Fe_2O_4$. Phys Rev B 8(1):29–43
Lv W-Z et al (2008) XRD studies on the nanosized copper ferrite powders synthesized by sonochemical method. J Alloy Compd 465(1–2):261–264
Maaz K et al (2007) Synthesis and magnetic properties of cobalt ferrite ($CoFe_2O_4$) nanoparticles prepared by wet chemical route. J Magn Magn Mater 308(2):289–295
Maia DF et al (2008) Influência dotipo de combustível na síntese por reação e combustão do catalisador ZnAl2O4. in 18 CBECiMat—Congresso Brasileiro de Engenharia e Ciências dos Materiais. Porto de Galinhas
Miyake A (1959) Infrared spectra of glycols coordinated to metal ions. Bull Chem Soc Jpn 32:1381–1383
Mohammed KA et al (2012) Infrared and structural studies of $Mg_{1-x}Zn_xFe_2O_4$ ferrites. Phys B 407(4):795–804
Mozaffari M et al (2010) The effect of solution temperature on crystallite size and magnetic properties of Zn substituted Co ferrite nanoparticles. J Magn Magn Mater 322(4):383–388
Paiva ACLA et al (2008) Síntese e caracterização de pós de ferrita Mn–Zn: efeito da substituição do Mn^{2+} pelo Fe^{2+} e da quantidade de H_2O. Revista Eletrônica de Materiais e Processos 3(1):25–30
Pérez JAL et al (1997) Advances in the preparation of magnetic nanoparticles by the microemulsion method. J Phys Chem B 101:8045–8047
Pérez-Mirabet L et al (2013) One-pot synthesis of stable colloidal solutions of MFe2O4 nanoparticles using oleylamine as solvent and stabilizer. Mater Res Bull 48(3):966–972
Poddar P et al (2005) Inter-particle interactions and magnetism in manganese–zinc ferrite nanoparticles. J Magn Magn Mater 288:443–451
Porto S (1981) Normal mode determination in crystals. J Raman Spectrosc 10:253–290
Poul L et al (2003) Synthesis of inorganic compounds (metal, oxide and hydroxide) in polyol medium: a versatile route related to the sol–gel process. J Sol-Gel Sci Technol 26(1–3):261–265
Raming TP et al (2002) The synthesis and magnetic properties of nanosized hematite (α-Fe_2O_3) particles. J Colloid Interface Sci 249(2):346–350
Ravinder D (1999) Far-infrared spectral studies of mixed lithium–zinc ferrites. Mater Lett 40(5):205–208
Reddy PV, Salagram M (1987) The far-infrared spectra of mixed manganese–magnesium ferrites. Phys Status Solidi (a) 100(2): 639–643
Rietveld HM (1967) Line profiles of neutron powder-diffraction peaks for structure refinement. Acta Crystallogr 22:151–152
Riman RE et al (2002) Solution synthesis of hydroxyapatite designer particulates. Solid State Ion 151(1–4):393–402
Sánchez RD et al (2002) Particle size effects on magnetic properties of yttrium iron garnets prepared by a sol–gel method. J Magn Magn Mater 247(1):92–98
Sato T et al (1987) Magnetic properties of ultrafine ferrite particles. J Magn Magn Mater 65(2–3):252–256
Sharifi I, Shokrollahi H, Amiri S (2012) Ferrite-based magnetic nanofluids used in hyperthermia applications. J Magn Magn Mater 324(6):903–915
Shebanova ON, Lazor P (2003) Raman spectroscopic study of magnetite ($FeFe_2O_4$): a new assignment for the vibrational spectrum. J Solid State Chem 174(2):424–430
Siddique M, Butt NM (2010) Effect of particle size on degree of inversion in ferrites investigated by Mossbauer spectroscopy. Phys B 405(19):4211–4215
Singhal S, Barthwal SK, Chandra K (2006) Structural, magnetic and Mossbauer spectral studies of nanosize aluminum substituted nickel zinc ferrites. J Magn Magn Mater 296(2):94–103
Sorescu M et al (2004) Hydrothermal synthesis and structural characterization of $(1-x)\alpha$-Fe_2O_3–$xSnO_2$ nanoparticles. J Phys Chem Solids 65(5):1021–1029
Srivastava M, Chaubey S, Ojha AK (2009) Investigation on size dependent structural and magnetic behavior of nickel ferrite nanoparticles prepared by sol–gel and hydrothermal methods. Mater Chem Phys 118(1):174–180
Suchanek WL, Riman RE (2006) Hydrothermal synthesis of advanced ceramic powders. Adv Sci Technol 45:184–193
Sugimoto M (1999) The past, present, and future of ferrites. J Am Ceram Soc 82(2):269–280

Thomas M, George KC (2009) Infrared and magnetic study of nanophase zinc ferrite. Indian J Pure Appl Phys 47:81–86

Upadhyay C et al (2003) Effect of preparation conditions on formation of nanophase Ni–Zn ferrites through hydrothermal technique. J Magn Magn Mater 260(1–2):188–194

Valenzuela R et al (2009) Influence of stirring velocity on the synthesis of magnetite nanoparticles (Fe3O4) by the co-precipitation method. J Alloy Compd 488(1):227–231

Velmurugan K, Venkatachalapathy VSK, Sendhilnathan S (2010) Synthesis of nickel zinc iron nanoparticles by coprecipitation technique. Mater Res 13(3):299–303

Waldron RD (1955) Infrared spectra of ferrites. Phys Rev 99(6):1727–1735

Wang L, Li FS (2001) Mossbauer study of nanocrystalline Ni–Zn ferrite. J Magn Magn Mater 223(3):233–237

Wang J et al (2009) Solvothermal synthesis and magnetic properties of size-controlled nickel ferrite nanoparticles. J Alloy Compd 479(1–2):791–796

Yáñez-Vilar S et al (2009) A simple solvothermal synthesis of MFe2O4 (M = Mn, Co and Ni) nanoparticles. J Solid State Chem 182(10):2685–2690

Ying JY et al (1992) STM/AFM study of grain boundary migration in nanostructured solids. Mater Lett 15(3):180–185

Zhang L, He R, Gu H-C (2006) Oleic acid coating on the monodisperse magnetite nanoparticles. Appl Surf Sci 253(5): 2611–2617

Zhang CF et al (2009) Effects of cobalt doping on the microstructure and magnetic properties of Mn–Zn ferrites prepared by the co-precipitation method. Phys B Condens Matter 404(16): 2327–2331